J. Fluid Mech. (2010), *vol.* 644, *pp.* 257–280.
doi:10.1017/S0022112009992394

Equilibrium magnetohydrodynamic flows of liquid metals in magnetorotational instability experiments

I. V. KHALZOV[1]†, A. I. SMOLYAKOV[2] AND V. I. ILGISONIS[3]

[1]Center for Magnetic Self-Organization, University of Wisconsin, 1150 University Avenue, Madison, WI 53706, USA

[2]University of Saskatchewan, 116 Science Place, Saskatoon, Saskatchewan, S7N5E2, Canada

[3]Russian Research Center 'Kurchatov Institute', 1 Kurchatov Square, Moscow, 123182, Russia

(Received 2 November 2008; revised 21 September 2009; accepted 22 September 2009)

A theoretical analysis of equilibrium magnetohydrodynamic flows in annular channels is performed from the perspective of establishing required conditions for liquid metal magnetorotational instability (MRI) experiments. Two different types of fluid rotation are considered: electrically driven flow in an annular channel and Taylor–Couette flow between rotating cylinders. The structure of these flows is studied within a unified approach as a function of the Hartmann and Reynolds numbers. The parameters appropriate for realization of MRI experiments are determined.

1. Introduction

The study of magnetohydrodynamic (MHD) flows in annular channels is of great current interest due to the experimental search for magnetorotational instability (MRI). MRI occurs when the angular velocity of the conducting fluid rotating in a transverse magnetic field decreases with radius (Velikhov 1959; Balbus & Hawley 1991), i.e.

$$\frac{\partial \Omega}{\partial R} < 0. \tag{1.1}$$

This condition is valid for many astrophysical objects (accretion disks, active galactic nuclei, etc.) where the rotation of matter obeys the Keplerian law $\Omega \propto R^{-3/2}$. Once magnetized the flow in these objects can become unstable through the mechanism of MRI. This results in different phenomena such as enhanced angular momentum transport and magnetic dynamo (Balbus & Hawley 1998; Balbus 2003; Silk & Langer 2006).

Because of the role played by MRI in astrophysics, a number of experiments have been initiated in recent years to test this instability in the laboratories (Noguchi *et al.* 2002; Noguchi & Pariev 2003; Ji *et al.* 2004; Sisan *et al.* 2004; Stefani *et al.* 2006; Velikhov *et al.* 2006*b*). The idea of these experiments is to drive the rotation of a conducting fluid (liquid metal or plasma) and investigate its stability in an external magnetic field. For implementation of the MRI experiment, it is crucial to achieve an initial equilibrium rotation profile, which can be unstable with respect to the MRI (1.1)

† Email address for correspondence: khalzov@wisc.edu

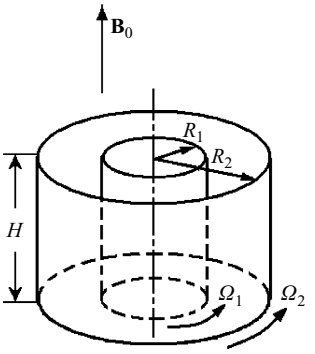

FIGURE 1. Sketch of magnetized TCF.

but is always stable to other instabilities (for example, hydrodynamical). The latter condition requires that the angular momentum per unit mass of rotating fluid increases as one moves radially outward. This is known as the Rayleigh stability criterion:

$$\frac{\partial(R^2\Omega)}{\partial R} \geqslant 0. \tag{1.2}$$

The rotation profiles satisfying both (1.1) and (1.2) are sometimes called quasi-Keplerian. They are the preferred initial background flows in MRI experiments.

Experimental observations of the MRI have been reported in two experiments (Sisan *et al.* 2004; Stefani *et al.* 2006). Sisan *et al.* (2004) reported observing the MRI in a spherical geometry on the background of an already turbulent flow. Stefani *et al.* (2006) reported detecting the so-called helical MRI in cylindrical flow in the combined axial and azimuthal magnetic fields. Helical MRI is currently the subject of intense discussions in the literature (Liu *et al.* 2006; Liu, Goodman & Ji 2007; Lakhin & Velikhov 2007; Rüdiger & Hollerbach 2007; Szklarski 2007; Stefani, Gailitis & Gerbeth 2008). The advantage of the helical MRI is that the presence of the azimuthal magnetic field reduces the instability threshold substantially (Hollerbach & Rüdiger 2005). Another way to reduce the MRI threshold in a cylindrical geometry is to use a non-uniform axial magnetic field (Ilgisonis & Khalzov 2007).

As for the standard MRI (i.e. MRI in cylindrical geometry with a uniform axial magnetic field), there has been no clear detection of this instability despite the numerous theoretical studies and attempts to observe it experimentally. This is due to several reasons, one of them being the difficulty of obtaining of quasi-Keperian flows in practice. In this paper we will focus on liquid metal equilibrium flows that are appropriate for experimental observation of the standard MRI.

Two different mechanisms of fluid rotation have been proposed for MRI experiments: mechanical drive by virtue of the viscous drag force acting on the fluid between rotating coaxial cylinders – the so-called Taylor–Couette flow or TCF (figure 1; Noguchi *et al.* 2002; Ji *et al.* 2004; Stefani *et al.* 2006), and electrical drive by the Ampere force arising when an electric current is passed through the fluid, which is in a transverse magnetic field – electrically driven flow or EDF (figure 2; Noguchi & Pariev 2003; Velikhov *et al.* 2006*b*). In most of the existing MRI experiments TCF is used. In the idealized case of infinitely long cylinders, TCF has the following radial profile of angular velocity:

$$\Omega(R) = a + \frac{b}{R^2}, \tag{1.3}$$

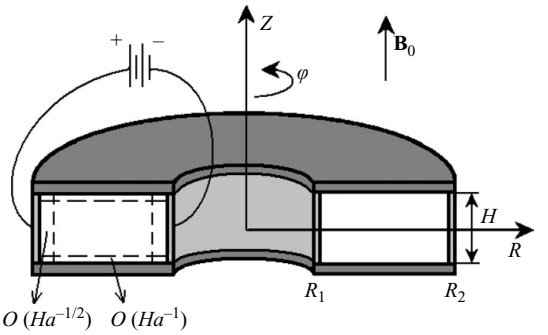

FIGURE 2. Sketch of EDF in an annular channel.

where the constants a and b are determined by the angular velocities of the cylinders and their radii. By adjusting these constants it is possible, in theory, to achieve a quasi-Keplerian flow. However, this situation is hard to realize experimentally, because in the real experiment the cylinders are bounded by the end plates (stationary or rotating). This affects the entire equilibrium flow, making its radial profile significantly different from the idealized one given by (1.3). As a result, the conditions for MRI may not be met and/or other parasitic instabilities (such as the Kelvin–Helmholtz instability) may be excited in the flow.

In the case of EDF, the flow forms the so-called Hartmann layers near the top and bottom walls and parallel boundary layers near the sidewalls of the channel. The widths of these layers scale with the Hartmann number, Ha (which is proportional to the external magnetic field; see (2.1)). By applying a large magnetic field, these boundary layers can be reduced considerably; then the bulk of the flow assumes a quasi-Keplerian rotation profile (Baylis & Hunt 1971)

$$\Omega(R) = \frac{C}{R^2}, \tag{1.4}$$

where the constant C is determined by the physical properties of the fluid and the total electric current passed through the channel. So, in any MRI experiment it is important to choose appropriate parameters in order to reduce the effect of the walls and keep the bulk of the flow uniform in the axial direction and quasi-Keplerian in the radial direction. This necessitates a theoretical analysis of equilibrium flow structure in the geometry relevant to MRI experiments.

The equilibrium structure of EDF in annular channels has been addressed in a number of papers (see, for example, Baylis & Hunt 1971; Pothérat, Sommeria & Moreau 2000; Khalzov & Smolyakov 2006). Baylis & Hunt (1971) studied equilibrium EDF analytically (neglecting the effect of inertia) and found a good agreement with experimental results. A quite general approach for the analytical description of MHD flows with small magnetic Prandtl numbers (a common property for liquid metals) in transverse magnetic field was proposed by Pothérat *et al.* (2000). Khalzov & Smolyakov (2006) developed a numerical method for calculating stationary MHD flows in channels with a rectangular cross-section. This method was used to find the structure of EDF for a particular set of parameters.

The equilibrium TCF between bounded cylinders in axial magnetic field has also been a subject of recent theoretical studies (see, for example, Kaneda *et al.* 2005; Tagawa & Kaneda 2005; Youd & Barenghi 2006; Szklarski & Rüdiger 2007; Liu 2008*a*). The majority of these studies deal with the MHD modification of

hydrodynamic Ekman layers induced in the flow by the end plates (Szklarski & Rüdiger 2007; Liu 2008*a*). At the same time, the effect of the magnetic field on TCF is global, it is not simply reduced to the development of new types of boundary layers. This effect remains poorly understood, although it is of primary importance to the success of MRI experiments.

In this paper, we perform a theoretical study of the equilibrium structure of both EDF and TCF within a unified approach as a function of the Hartmann and Reynolds numbers. Our main analytical results are obtained by employing the method of Pothérat *et al.* (2000), while numerical simulations are based on the procedure proposed by Khalzov & Smolyakov (2006). The structure of the paper is the following. In § 2, we formulate the problem of finding an axisymmetric incompressible MHD flow in an annular channel. Section 3 gives an outline of the numerical method developed by Khalzov & Smolyakov (2006). In § 4, the EDF of liquid metal is considered. Section 5 deals with Taylor–Couette flow in an axial magnetic field and its possible regimes. In § 6 we summarize the conditions that have to be satisfied in both cases to realize the rotation profiles appropriate for MRI experiments.

2. Statement of the problem

We consider the problem of finding the equilibrium flow of liquid metal in an annular channel with a rectangular cross-section. At this point, the mechanism of flow drive is not specified: it can be either TCF (figure 1) or EDF (figure 2). This mechanism is specified below by an appropriate choice of boundary conditions.

The channel is an axisymmetric toroid with inner radius R_1, outer radius R_2 and height H. Its axis of symmetry coincides with the Z axis of the cylindrical coordinate system $\{R, \varphi, Z\}$. In order to simplify consideration, we make the following assumptions:

(i) liquid metal completely fills the channel; its density ρ, kinematic viscosity ν and electric conductivity σ are constant throughout the entire volume;

(ii) the channel is placed into an external uniform magnetic field directed along the Z axis, $\boldsymbol{B}_0 = B_0 \boldsymbol{e}_z$;

(iii) the magnetic field induced by currents in the liquid metal is negligible compared with the externally applied field $\boldsymbol{B}_0$ (inductionless approximation);

(iv) the equilibrium flow is axisymmetric, i.e. for any physical quantity $\partial/\partial\varphi = 0$.

Formally, inductionless approximation (assumption iii) is applicable when the magnetic Reynolds number is small, $Re_m \ll 1$ (Müller & Bühler 2001). However, in the problem under consideration, this condition can be relaxed for large Hartmann numbers, $Ha \gg 1$. As shown by Khalzov & Smolyakov (2006), for EDF the ratio of induced magnetic field to the external one is about Re_m/Ha, so the inductionless approximation is valid if $Re_m \ll Ha$. Here, and in the rest of the paper, we use the following definitions of the Reynolds, magnetic Reynolds and Hartmann numbers:

$$Re = \frac{L_0 V_0}{\nu}, \quad Re_m = \mu_0 \sigma L_0 V_0, \quad Ha = L_0 B_0 \sqrt{\frac{\sigma}{\rho \nu}}, \tag{2.1}$$

where μ_0 is the vacuum permeability, $L_0 = H/2$ is a unit of length, B_0 is the magnitude of the applied magnetic field and V_0 is the characteristic value of velocity that will be specified below, depending on the type of the flow.

The equilibrium flow of liquid metal is described by incompressible dissipative MHD equations. In inductionless approximation, they are (Müller & Bühler 2001)

$$\nabla \cdot \boldsymbol{v} = 0, \tag{2.2}$$

$$\nabla \cdot \boldsymbol{j} = 0, \tag{2.3}$$

$$Re\,(\boldsymbol{v} \cdot \nabla)\boldsymbol{v} = -\nabla p + Ha\,\boldsymbol{j} \times \boldsymbol{b}_0 + \nabla^2 \boldsymbol{v}, \tag{2.4}$$

$$\boldsymbol{j} = -\nabla \phi + Ha\,\boldsymbol{v} \times \boldsymbol{b}_0. \tag{2.5}$$

Here, $\boldsymbol{b}_0$, $\boldsymbol{v}$, $\boldsymbol{j}$, p, ϕ stand for applied magnetic field, velocity, current density, pressure, and electric potential, scaled by B_0, V_0, $J_0 = \sigma V_0 B_0/Ha$, $P_0 = \rho V_0^2/Re$ and $\Phi_0 = L_0 V_0 B_0/Ha$, respectively. As one can see, the solution to the system (2.2)–(2.5) depends only on two dimensionless parameters – Reynolds and Hartmann numbers.

In the case of axial symmetry (assumption iv), it is convenient to represent the normalized velocity $\boldsymbol{v}$ and current density $\boldsymbol{j}$ in the form, automatically satisfying divergence-free conditions (2.2) and (2.3):

$$\boldsymbol{v} = \frac{1}{r}\nabla w(r, z) \times \boldsymbol{e}_\varphi + \frac{u(r, z)}{r}\,\boldsymbol{e}_\varphi,$$

$$\boldsymbol{j} = \frac{1}{r}\nabla h(r, z) \times \boldsymbol{e}_\varphi + \frac{g(r, z)}{r}\,\boldsymbol{e}_\varphi,$$

where $r = R/L_0$ and $z = Z/L_0$ are scaled coordinates, functions w and h are poloidal stream functions of the velocity and the current density, and functions u and g represent angular momentum of the fluid and 'momentum' of the toroidal current density, respectively. Substituting these expressions into (2.4) and (2.5), one obtains after some mathematical manipulations:

$$0 = \Delta^* u + Ha\frac{\partial h}{\partial z} + \frac{Re}{r}\,[u, w], \tag{2.6}$$

$$0 = \Delta^* h + Ha\frac{\partial u}{\partial z}, \tag{2.7}$$

$$0 = \Delta^*\Delta^* w - Ha^2\frac{\partial^2 w}{\partial z^2} - Re\left(r\left[w, \frac{\Delta^* w}{r^2}\right] + \frac{1}{r^2}\frac{\partial u^2}{\partial z}\right), \tag{2.8}$$

$$g = Ha\frac{\partial w}{\partial z}, \tag{2.9}$$

where the following notation is used

$$[f, g] \equiv \frac{\partial f}{\partial r}\frac{\partial g}{\partial z} - \frac{\partial f}{\partial z}\frac{\partial g}{\partial r}, \quad \Delta^* = r\frac{\partial}{\partial r}\frac{1}{r}\frac{\partial}{\partial r} + \frac{\partial^2}{\partial z^2}.$$

System (2.6)–(2.9) is the basis for our analysis of equilibrium axisymmetric MHD flow of a liquid metal in an annular channel.

System (2.6)–(2.9) has to be solved for adequate hydrodynamic and electric boundary conditions. The standard hydrodynamic boundary condition is

$$\boldsymbol{v}|_S = \boldsymbol{v}^{(w)}|_S, \tag{2.10}$$

where $\boldsymbol{v}^{(w)}$ is the velocity of the wall, and S denotes the fluid–wall interface, which in our case is $S = \{z = \pm 1$ (top and bottom walls), $r = r_{1,2} = R_{1,2}/L_0$ (sidewalls)$\}$.

The boundary conditions for the electric current density $\boldsymbol{j}$ are determined by the conductivity of the channel walls. In this study, we assume that the top and bottom walls of the channel are insulating, while the sidewalls are perfectly conducting

for both EDF and TCF. Normal components of the current density vanish at the insulating walls,

$$j_z|_{z=\pm 1} = 0. \tag{2.11}$$

At the interface between fluid and perfectly conducting walls the potential becomes uniform, leading to the absence of tangential components of the current density

$$j_z|_{r=(r_1,r_2)} = 0, \quad j_\varphi|_{r=(r_1,r_2)} = 0 \tag{2.12}$$

Conditions (2.11) and (2.12) can be combined to give a boundary condition for the poloidal current stream function h:

$$\left.\frac{\partial h}{\partial r}\right|_S = 0. \tag{2.13}$$

The toroidal current function g is completely determined by (2.9).

We note that the geometry of the problem implies symmetry with respect to the plane $z = 0$. Therefore, the unknown functions are either even or odd functions of z. In our study we take u and g to be even and h and w to be odd functions of z. These requirements are consistent with system (2.6)–(2.9) and corresponding boundary conditions.

3. Numerical method

In this section, we outline a numerical method developed by Khalzov & Smolyakov (2006) for solving systems of two-dimensional elliptical equations. This is a finite-difference method using the well-known iterative Jacobi algorithm with checkerboard updating of the grid function and successive over-relaxation (see, for example, Press *et al.* 1992). For system (2.6)–(2.8) the iterative scheme is

$$\boldsymbol{y}_{i,j}^{n+1} = (1-\mu)\boldsymbol{y}_{i,j}^{n} + \frac{1}{4}\mu\left[\left(1-\frac{s}{2r_i}\right)\boldsymbol{y}_{i+1,j}^{n} + \left(1+\frac{s}{2r_i}\right)\boldsymbol{y}_{i-1,j}^{n} + \boldsymbol{y}_{i,j+1}^{n} + \boldsymbol{y}_{i,j-1}^{n} + s^2\boldsymbol{f}_{i,j}(\boldsymbol{y}^n, r)\right], \tag{3.1}$$

where $\boldsymbol{y}$ is an unknown vector function

$$\boldsymbol{y}(r,z,t) = \begin{pmatrix} u(r,z,t) \\ h(r,z,t) \\ \tilde{w}(r,z,t) \\ w(r,z,t) \end{pmatrix},$$

$\boldsymbol{f}$ is a source vector function

$$\boldsymbol{f}(\boldsymbol{y}, r) = \begin{pmatrix} -Ha\dfrac{\partial h}{\partial z} - \dfrac{Re}{r}\,[u, w] \\ -Ha\dfrac{\partial u}{\partial z} \\ Ha^2\dfrac{\partial w}{\partial z^2} + Re\left(r\left[w, \dfrac{\tilde{w}}{r^2}\right] + \dfrac{1}{r^2}\dfrac{\partial u^2}{\partial z}\right) \\ \tilde{w} \end{pmatrix},$$

μ is the relaxation parameter and s is the grid spacing (equal in r- and z-directions).

	R_1 (cm)	R_2 (cm)	H (cm)	Fluid	Ha	Re
Obninsk	3	15	6	Na	100	$0–1.4\times10^6$
Princeton	7	21	28	Ga	0–3100	$0–6.3\times10^6$

TABLE 1. Parameters of the Obninsk and Princeton MRI experiments.

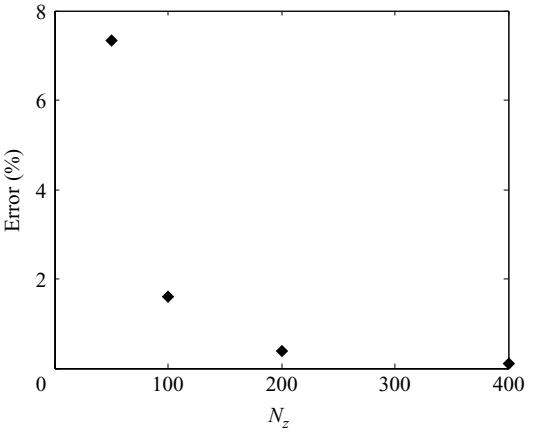

FIGURE 3. Deviation of numerically calculated value of u from its analytical value (4.8) at $z = 0.96$ for different number of grid points in the z-direction. Numerical calculations are performed using reduced system (4.6) and (4.7) for $Ha = 30$.

Based on the iterative scheme (3.1), Khalzov & Smolyakov (2006) implemented a numerical code in C++ for the calculations of the equilibrium axisymmetric MHD flows in annular channels with rectangular cross-section. We used this code to obtain the results reported here. In our simulations, the relaxation parameter μ was chosen by the trial and error method to ensure the convergence of the iterations. The grid was uniform with spacing $s = 0.02$ in both directions; this corresponded to $N_z = 100$ grid points in the z-direction and $N_r = 50$ (for TCF) or $N_r = 200$ (for EDF) grid points in the r-direction. This was enough to resolve all boundary layers; besides, our test runs with higher resolution did not show much difference (see figure 3). The accuracy of the obtained results is also demonstrated in figures 5(i.*d*, ii.*d*) and 8(i.*d*, ii.*d*, iii.*d*), where the balance of different terms of (2.6) is shown.

4. Electrically driven flow

In this section, we study a liquid metal flow driven by imposed electric current in the presence of a transverse magnetic field (figure 2). The study is performed for the geometry of the Obninsk MRI experiment proposed by Velikhov *et al.* (2006*b*) (table 1): normalized radii of inner and outer cylinders are $r_1 = R_1/L_0 = 1$ and $r_2 = R_2/L_0 = 5$, respectively, where $H = 2L_0$ is the height of the channel. In order to describe the characteristic features of this type of flow, we consider the flow at Hartmann and Reynolds numbers different from those expected in the Obninsk experiment. The analytical part of our study is based on the method of Pothérat *et al.* (2000), who used the averaging of the force-balance equation along the magnetic field lines.

4.1. *Boundary conditions for electrically driven flow*

In EDF, all channel walls are stationary, so $\boldsymbol{v}|_S = 0$ (2.10). Taking into account the oddness of the poloidal velocity stream function w with respect to z, we obtain

$$u|_S = 0, \tag{4.1}$$

$$w|_S = 0, \quad \left.\frac{\partial w}{\partial r}\right|_{r=(r_1,r_2)} = 0, \quad \left.\frac{\partial w}{\partial z}\right|_{z=\pm 1} = 0. \tag{4.2}$$

The boundary conditions for the poloidal current stream function h follow from (2.13), which means that h is constant at the top and bottom channel walls, i.e. $h|_{z=\pm 1} = \pm h_0$ (h is odd function of z). This constant is related to the total electric current I_0 flowing through the fluid. Indeed, the total radial current in an arbitrary section $R = \text{const}$ of the channel is

$$I_0 = -J_0 L_0^2 \int_{-1}^{1} 2\pi r j_r \mathrm{d}z = \frac{4\pi L_0 B_0 Re_m}{\mu_0 Ha} h_0. \tag{4.3}$$

The positive sign of the total current, $I_0 > 0$, corresponds to a current flowing from the outer channel wall to the inner one. As discussed by Khalzov & Smolyakov (2006), for EDF it is convenient to choose $h_0 = 1$, i.e.

$$\left.\frac{\partial h}{\partial r}\right|_{r=(r_1,r_2)} = 0, \quad h|_{z=\pm 1} = \pm 1. \tag{4.4}$$

Then the value $h(r, z)$ shows the part of the total current flowing between planes $-z$ and z at a given radius r. Moreover, from (4.3) one obtains the characteristic value of angular momentum (per unit mass) of the EDF

$$M_0 \equiv L_0 V_0 = \frac{I_0}{4\pi\sqrt{\rho\sigma\nu}}. \tag{4.5}$$

It should be stressed here that the characteristic value of the angular momentum (4.5) is independent of the magnetic field. The Reynolds number in EDF is proportional to the total current:

$$Re \equiv \frac{M_0}{\nu} = \frac{I_0}{4\pi\nu\sqrt{\rho\sigma\nu}}.$$

Such definition of Re is very convenient since it is not related to a particular structure of flow.

Equations (4.1), (4.2) and (4.4) constitute a complete set of boundary conditions for EDF.

4.2. *Hartmann flow*

First, we consider EDF in the central part of the channel far from the sidewalls. In this case, one can neglect the radial dependence of flow parameters ($\partial/\partial r \to 0$), then system (2.6)–(2.9) is reduced to equations

$$0 = \frac{\partial^2 u}{\partial z^2} + Ha\frac{\partial h}{\partial z}, \tag{4.6}$$

$$0 = \frac{\partial^2 h}{\partial z^2} + Ha\frac{\partial u}{\partial z}. \tag{4.7}$$

The same system of equations is obtained in the analysis of the equilibrium liquid metal flow between two infinite plates in a transverse magnetic field –

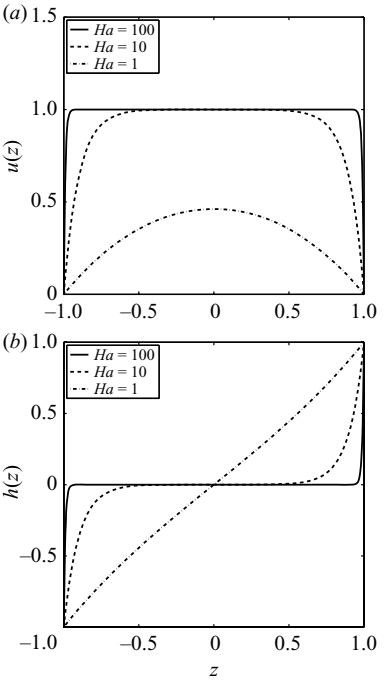

FIGURE 4. Hartmann flow: (*a*) normalized angular momentum (4.8) and (*b*) poloidal current stream function (4.9) at different values of the Hartmann number Ha.

the so-called Hartmann flow (Müller & Bühler 2001). The difference is only in the physical meaning of the functions u and h: for Hartmann flow they are normalized components of velocity and induced magnetic field, respectively; for annular channel they are normalized angular momentum of the fluid, $u = rv_\varphi$, and poloidal current stream function (or 'momentum' of azimuthal magnetic field), $h = rb_\varphi$. Such analogy between the angular momentum and the velocity in straight geometry is well known in the literature (see, for example, Heiser & Shercliff 1965).

The exact solution to system (4.6) and (4.7) satisfying boundary conditions (4.1) and (4.4) is

$$u(z) = \frac{\cosh Ha - \cosh(Ha\, z)}{\sinh Ha}, \tag{4.8}$$

$$h(z) = \frac{\sinh(Ha\, z)}{\sinh Ha}. \tag{4.9}$$

These dependencies are shown in figure 4 for different values of the Hartmann number. At large Hartmann numbers $Ha \gg 1$, the flow develops the boundary layers of thickness $O(Ha^{-1})$ – the so-called Hartmann layers.

The Hartmann profile of angular momentum (4.8) is of crucial importance in the study of equilibrium MHD flows in annular channels. As shown below, at large Hartmann numbers, the z-dependence of angular momentum in both electrically driven and Taylor–Couette flows is very well approximated by (4.8).

4.3. *Radial profile of angular momentum*

For large Hartmann numbers the angular momentum of electrically driven fluid in an annular channel can be described by the expression

$$u(r,z) = u_0(r)\frac{\cosh Ha - \cosh(Ha\, z)}{\sinh Ha}, \tag{4.10}$$

which takes into account the presence of the Hartmann layers in the flow and assumes some radial dependence $u_0(r)$ of the angular momentum in the core region. Approximation (4.10) is verified by the following analysis and numerical simulations.

The equation that governs the radial profile of the angular momentum $u_0(r)$ was obtained by Pothérat *et al.* (2000), who used the averaging of the force-balance equation in z-direction (along the magnetic field lines):

$$\frac{\partial^2 u_0}{\partial r^2} - \frac{1}{r}\frac{\partial u_0}{\partial r} - Hau_0 + Ha - \frac{7Re^2}{36rHa^3}\frac{\partial}{\partial r}\left(\frac{u_0^3}{r^2}\right) = 0. \tag{4.11}$$

This equation has a clear physical meaning. The first three terms describe the z-averaged viscous friction due to non-uniformity of the angular momentum. The fourth term is the Ampere force (electrical drive), which is proportional to the total current flowing through the channel. The last term is the inertia; it expresses nonlinear radial transport of angular momentum by the secondary (poloidal) flows.

Depending on the relative values of the viscous, Ampere and inertial forces, two flow regimes are realized. Simple estimates show that the inertia in (4.11) can be neglected if (Baylis & Hunt 1971)

$$Re \ll Ha^2\left(\frac{R_1}{H}\right)^2. \tag{4.12}$$

This is the so-called inertialess regime. In this regime, viscous forces near the channel walls are balanced by the Ampere force. The case of the opposite inequality corresponds to the *inertial* flow, in which all forces are comparable. In the subsequent sections we consider these two regimes in more details.

4.4. *Inertialess regime*

If condition (4.12) is satisfied, the nonlinear term in (4.11) can be neglected:

$$\frac{\partial^2 u_0}{\partial r^2} - \frac{1}{r}\frac{\partial u_0}{\partial r} - Hau_0 + Ha = 0. \tag{4.13}$$

This ordinary differential equation possesses an exact solution which is expressed in terms of the modified Bessel function of the first kind:

$$u_0(r) = 1 - \frac{r}{I_1(\sqrt{Ha}(r_2 - r_1))}\left[\frac{1}{r_1} I_1(\sqrt{Ha}(r_2 - r)) + \frac{1}{r_2} I_1(\sqrt{Ha}(r - r_1))\right], \tag{4.14}$$

where the boundary condition (4.1) is taken into account. The dependence (4.14) is simplified near the walls at $r = r_{1,2}$, namely:

$$u_0(x) \approx 1 - \exp(-\sqrt{Ha}\, x), \tag{4.15}$$

where $x = |r - r_{1,2}|$ is a non-dimensional distance measured from the corresponding wall. We note that (4.15) describes the side boundary layers of thickness $O(Ha^{-1/2})$ (they are known as parallel layers). If $r_2 - r_1 \gg Ha^{-1/2}$ or, in other words, if

$$R_2 - R_1 \gg \frac{H}{\sqrt{Ha}}, \tag{4.16}$$

then these layers are small compared with the channel width and the normalized angular momentum is close to 1 in the most part of the flow. In this case, the angular velocity of EDF in the channel can be approximated as (in dimensional units)

$$\Omega(R) = \frac{M_0}{R^2}, \tag{4.17}$$

where M_0 is defined by (4.5). Such rotation is quasi-Keplerian and suitable for MRI experiments.

The calculated structure of EDF in inertialess regime ($Re = 10$, $Ha = 30$) is presented in figure 5(i.*a–d*). From figure 5(i.*a*) one can see that the normalized angular momentum is equal to 1 almost entirely in the cross-section of the channel with the exception of boundary layers near the walls. This result is in a good agreement with (4.10) and (4.14); the comparison is shown in figure 6.

The electric current lines (contours of the function $h(r, z)$) are shown in figure 5(i.*c*). At large Hartmann numbers, almost all the current in electrically driven fluid is expelled to the top and bottom walls and flows through the thin Hartmann layers.

The balance of different terms in (2.6) in the mid-plane of the channel (at $z = 0$) is presented in figure 5(i.*d*). In inertialess regime the bulk of EDF is force-free, and only in the parallel boundary layers viscosity is balanced by the Ampere force.

4.5. *Effect of inertia*

Now we consider the influence of inertia (the nonlinear term in (4.11)) on the radial profile of angular momentum $u_0(r)$ assuming that (4.12) is violated, i.e.

$$Re \approx Ha^2 \left(\frac{R_1}{H}\right)^2.$$

This influence is most important in the region of the parallel layers near the walls at $r = r_{1,2}$. As shown by Pothérat *et al.* (2000), in this case the non-dimensional width of the parallel layers can be approximated by

$$\delta_1 \approx \frac{Re^2}{r_1^3 Ha^4} \tag{4.18}$$

for the inner wall, and by

$$\delta_2 \approx \frac{r_2^3 Ha^3}{Re^2} \tag{4.19}$$

for the outer wall. Thus, if inertia is large, the inner parallel layer (4.18) penetrates the bulk of the flow forming poloidally rotating vortices. As a result, the rotation profile is changed significantly and the conditions for MRI excitation may not be met. This precludes the use of the inertial EDF in MRI experiment. The outer parallel layer, on the contrary, decreases with growth of the Reynolds number according to (4.19).

The calculated equilibrium structure of EDF in inertial regime ($Re = 4000$, $Ha = 30$) is shown in figure 5(ii.*a–d*). The typical feature of the flow in inertial regime is the development of two poloidal circulation cells (figure 5ii.*b*). Their presence leads to a coupling of the azimuthal velocity component with radial and axial ones (inertial effects). These effects result in a change of the angular momentum profile (figure 5ii.*a*) and modification of the force balance (figure 5ii.*d*).

The radial profiles of the angular momentum u for different values of Reynolds number are presented in figure 7(*a*). As follows from this figure, with growth of Re,

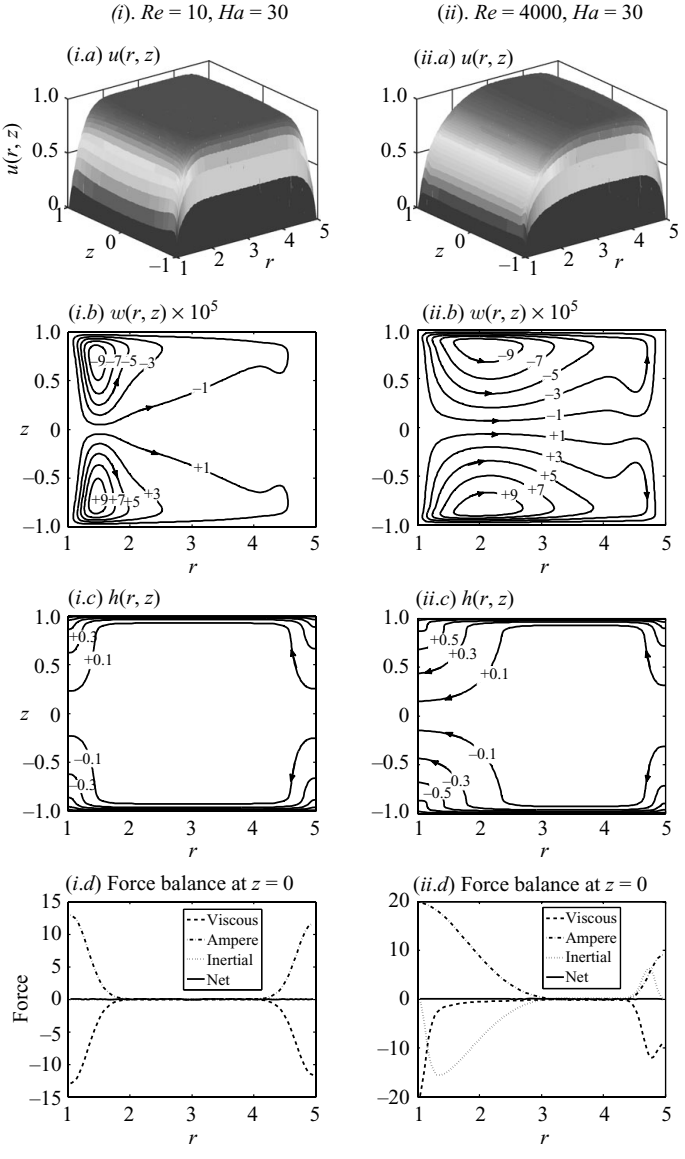

FIGURE 5. Calculated structure of EDF in (*i*) inertialess ($Re = 10$, $Ha = 30$) and (*ii*) inertial ($Re = 4000$, $Ha = 30$) regimes: (*a*) normalized angular momentum $u(r, z)$; (*b*) poloidal circulation lines (contours of $w(r, z)$); (*c*) electric current lines (contours of $h(r, z)$); (*d*) balance of toroidal forces in the mid-plane of the channel at $z = 0$. Calculations are performed using the full system (2.6)–(2.8).

the boundary layer increases near the inner wall of the channel and decreases near the outer wall. Such behaviour of the parallel boundary layers is qualitatively described by (4.18) and (4.19).

Our numerical simulations show that the dependence of the angular momentum in the Hartmann layers near the top and bottom walls of the channel remains practically the same for the wide range of Reynolds numbers (figure 7*b*) and corresponds to the Hartmann flow profile (4.8). This validates the use of representation (4.10).

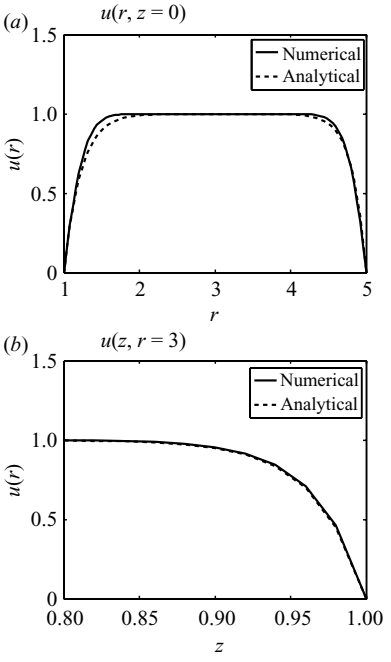

FIGURE 6. Comparison of calculated angular momentum profile $u(r, z)$ (solid lines) with analytical approximation given by (4.10) and (4.14) (dashed lines) in inertialess regime of EDF ($Re = 10$, $Ha = 30$): (a) in the mid-plane of the channel at $z = 0$; (b) in the Hartmann layer at $r = 3$.

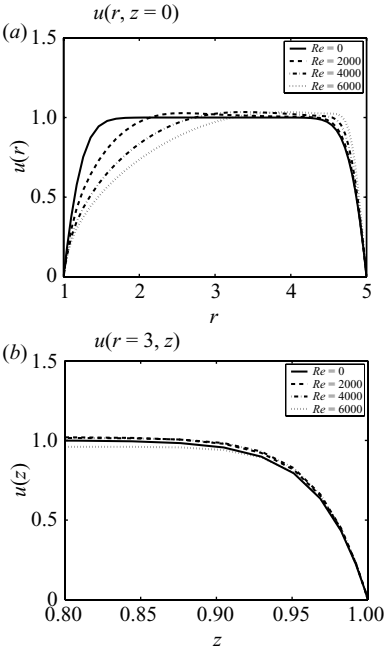

FIGURE 7. Calculated profiles of normalized angular momentum $u(r, z)$ in EDF for different values of Re at $Ha = 30$: (a) in the mid-plane of the channel at $z = 0$; (b) in the Hartmann layer at $r = 3$.

5. Taylor–Couette flow

In this section, we perform a theoretical study of a liquid metal flow between two coaxial rotating cylinders (figure 1) placed in an axial magnetic field. We demonstrate characteristic features of TCF at different values of the Reynolds and Hartmann numbers in the geometry of the Princeton MRI experiment (table 1): normalized radii of inner and outer cylinders are $r_1 = R_1/L_0 = 0.5$ and $r_2 = R_2/L_0 = 1.5$, respectively, where $H = 2L_0$ is the height of the channel. We also analyse the effect of the split end caps on the TCF. For simplicity, we assume that end caps are insulating, cylinders are perfectly conducting and both cylinders are rotating with the same angular momentum, i.e. $\Omega_1 R_1^2 = \Omega_2 R_2^2 = M_0$. These assumptions still provide quite general results; moreover, they allow comparison of TCF with EDF (which is, roughly speaking, a flow with constant angular momentum; see (4.17)). The effect of the conductivity of the channel walls on the TCF is not considered here and will be published elsewhere.

5.1. *Boundary conditions for Taylor–Couette flow*

In the case of TCF, the boundary conditions for velocity components are analogous to those in EDF ((4.1) and (4.2)):

$$u|_{r=(r_1,r_2)} = u_{1,2}, \quad u|_{z=\pm 1} = 0, \tag{5.1}$$

$$\left.\frac{\partial w}{\partial r}\right|_{r=(r_1,r_2)} = 0, \quad \left.\frac{\partial w}{\partial z}\right|_{z=\pm 1} = 0, \quad w|_S = 0, \tag{5.2}$$

where u_1 and u_2 are non-dimensional angular momenta corresponding to rotating inner and outer walls, i.e.

$$u_1 = \frac{M_1}{M_0} = \frac{\Omega_1 R_1^2}{M_0}, \quad u_2 = \frac{M_2}{M_0} = \frac{\Omega_2 R_2^2}{M_0}.$$

Here, M_0 is the characteristic angular momentum. It can be chosen to be equal to either M_1 or M_2, whichever is not zero.

Assuming insulating end plates and perfectly conducting cylinders, we arrive at the boundary conditions for the poloidal current stream function $h(r, z)$, which are similar to (4.4)

$$\left.\frac{\partial h}{\partial r}\right|_{r=(r_1,r_2)} = 0, \quad h|_{z=\pm 1} = 0. \tag{5.3}$$

The last condition takes into account the fact that the total electric current between the cylinders is absent.

The structure of TCF is determined completely by system (2.6)–(2.9) and boundary conditions (5.1–5.3).

5.2. *Boundary layers near end plates*

It is well known that TCF is strongly affected by the boundary layers developed near the top and bottom end plates (Acheson & Hide 1973; Davidson & Pothérat 2002; Hollerbach & Fournier 2004; Kageyama *et al.* 2004; Szklarski & Rüdiger 2007; Liu 2008*a*). The thickness of these boundary layers can be obtained from force-balance equation (2.4). Indeed, for the azimuthal component of this equation, we have the following estimates of the terms near the end plates:

$$O\left(\frac{1}{\delta_z^2}\right) + O(\Gamma^2) = O\left(\frac{Re}{r_1^2}\right) + O(Ha^2), \tag{5.4}$$

where $\Gamma = H/(R_2 - R_1)$ is the aspect ratio of the channel, the left-hand side characterizes viscous forces and two terms on the right-hand side characterize inertia and Ampere force, respectively. Depending on the relative values of Γ, Re and Ha, three basic types of boundary layers are possible; they correspond to three different regimes of TCF:

(i) *viscous regime* with *viscous layers* of width

$$\delta_{visc} \approx \frac{1}{\Gamma} \approx r_2 - r_1;$$

(ii) *inertial regime* with *Ekman layers* of width

$$\delta_{Ek} \approx \frac{r_1}{\sqrt{Re}};$$

(iii) *magnetized regime* with *Hartmann layers* of width

$$\delta_{Ha} \approx \frac{1}{Ha}.$$

Below, we consider these regimes in more detail.

5.3. *Viscous regime*

In the viscous regime, when $Re \ll \Gamma r_1$ and $Ha \ll \Gamma$, we can assume $Ha = 0$ and $Re = 0$, so system (2.6)–(2.9) is reduced to one equation

$$\frac{\partial^2 u}{\partial r^2} - \frac{1}{r}\frac{\partial u}{\partial r} + \frac{\partial^2 u}{\partial z^2} = 0. \tag{5.5}$$

Strictly speaking, the case of $Re = 0$ presumes no rotation at all; it is physically meaningful to consider it only as the limit of small Reynolds numbers, $Re \to 0$. Equation (5.5) with boundary conditions (5.1) can be solved exactly in terms of infinite series (Wendl 1999). In a small gap approximation ($r_2 - r_1 \ll r_{1,2}$), the solution has the form

$$u(r,z) = \frac{u_1 r_2^2 - u_2 r_1^2}{r_2^2 - r_1^2} + \frac{u_2 - u_1}{r_2^2 - r_1^2}\, r^2 + \sum_{j=1}^{\infty} a_j \sin\left[2jk_r\left(r - \frac{r_1 + r_2}{2}\right)\right]\frac{\cosh[2jk_r z]}{\cosh[2jk_r]}$$
$$+ \sum_{j=0}^{\infty} b_j \cos\left[(2j+1)k_r\left(r - \frac{r_1 + r_2}{2}\right)\right]\frac{\cosh[(2j+1)k_r z]}{\cosh[(2j+1)k_r]}, \tag{5.6}$$

where

$$k_r = \frac{\pi}{r_2 - r_1},$$

and the coefficients a_j and b_j are

$$a_j = \frac{(-1)^j (u_2 - u_1)}{\pi j},$$
$$b_j = -\frac{2(-1)^j (u_1 + u_2)}{\pi(2j+1)} + \frac{8(-1)^j (u_2 - u_1)(r_2 - r_1)}{\pi^3 (2j+1)^3 (r_1 + r_2)}.$$

Equation (5.6) is simplified if we consider a rotation with $u_1 = u_2 = 1$. In this case, the r-profile of the normalized angular momentum u in the mid-plane of the channel at $z = 0$ can be approximated as

$$u(r) \approx 1 - \frac{4\cos[k_r(r - (r_1 + r_2)/2)]}{\pi \cosh k_r}, \tag{5.7}$$

while the z-profile of u in the middle section of the channel at $r=(r_1+r_2)/2$ is approximated as

$$u(z) \approx 1 - \frac{\cosh[k_r z]}{\cosh k_r}. \tag{5.8}$$

The calculated structure of TCF in viscous regime ($Re=1$, $Ha=1$) for $u_1=u_2=1$ is shown in figure 8(i.*a–d*). In these simulations, values of Re and Ha are taken small but finite to have functions w and h not equal to zero identically. As one can see, the normalized angular momentum is almost 1 in the central part of the cross-section of the channel and decreases to 0 in the viscous boundary layers near the end plates. This result is in a good agreement with (5.7) and (5.8); the comparison is shown in figure 9. Thus, we conclude that the viscous TCF is appropriate for MRI experiments if the boundary layers are less than the height of the channel or, in other words, if

$$R_2 - R_1 \lesssim H. \tag{5.9}$$

5.4. *Inertial regime*

In the inertial regime, when $Re \gg \Gamma^2 r_1^2$ and $Re \gg Ha^2 r_1^2$, we can neglect the magnetic field, so system (2.6)–(2.9) becomes

$$0 = \Delta^* u + \frac{Re}{r}[u, w],$$
$$0 = \Delta^*\Delta^* w - Re\left(r\left[w, \frac{\Delta^* w}{r^2}\right] + \frac{1}{r^2}\frac{\partial u^2}{\partial z}\right).$$

The analytical treatment of such system is quite difficult since the equations are essentially nonlinear. In this section we discuss only the numerical results for the case $u_1=u_2=1$.

The equilibrium structure of the inertial TCF ($Re=500$, $Ha=1$) is presented in figure 8(ii.*a–d*). We take a small but finite value of Ha to demonstrate the distribution of the current in this regime (if $Ha=0$, then $h=0$ identically). One of the typical features of high-Re Taylor–Couette flow is the existence of the jet-like formation near the mid-plane (at $z=0$) of the azimuthal momentum profile u (figure 8ii.*a*). It is undoubtedly the counterpart of the strong radial outflow that is seen in figure 8(ii.*b*). Such jet-like structures in the flow are explained by the presence of the steady end plates (Ji *et al.* 2004; Kageyama *et al.* 2004).

These results suggest that the inertial regime of TCF is of little use in the MRI experiments. The instabilities one obtains in this regime (even with magnetic field) will most probably be the familiar Kelvin–Helmholtz instabilities of the jet-like structures, rather than the magnetorotational instability. At best, one might hope to obtain the MRI superimposed on these Kelvin–Helmholtz modes. Any subsequent interpretation of experimental results will be quite complicated.

5.5. *Magnetized regime*

The magnetized regime of TCF is realized when $Ha \gg \Gamma$ and $Ha^2 r_1^2 \gg Re$. It is formally described by system (2.6)–(2.9) in the limit of small Reynolds numbers, $Re \to 0$:

$$0 = \Delta^* u + Ha\frac{\partial h}{\partial z}, \tag{5.10}$$

$$0 = \Delta^* h + Ha\frac{\partial u}{\partial z}. \tag{5.11}$$

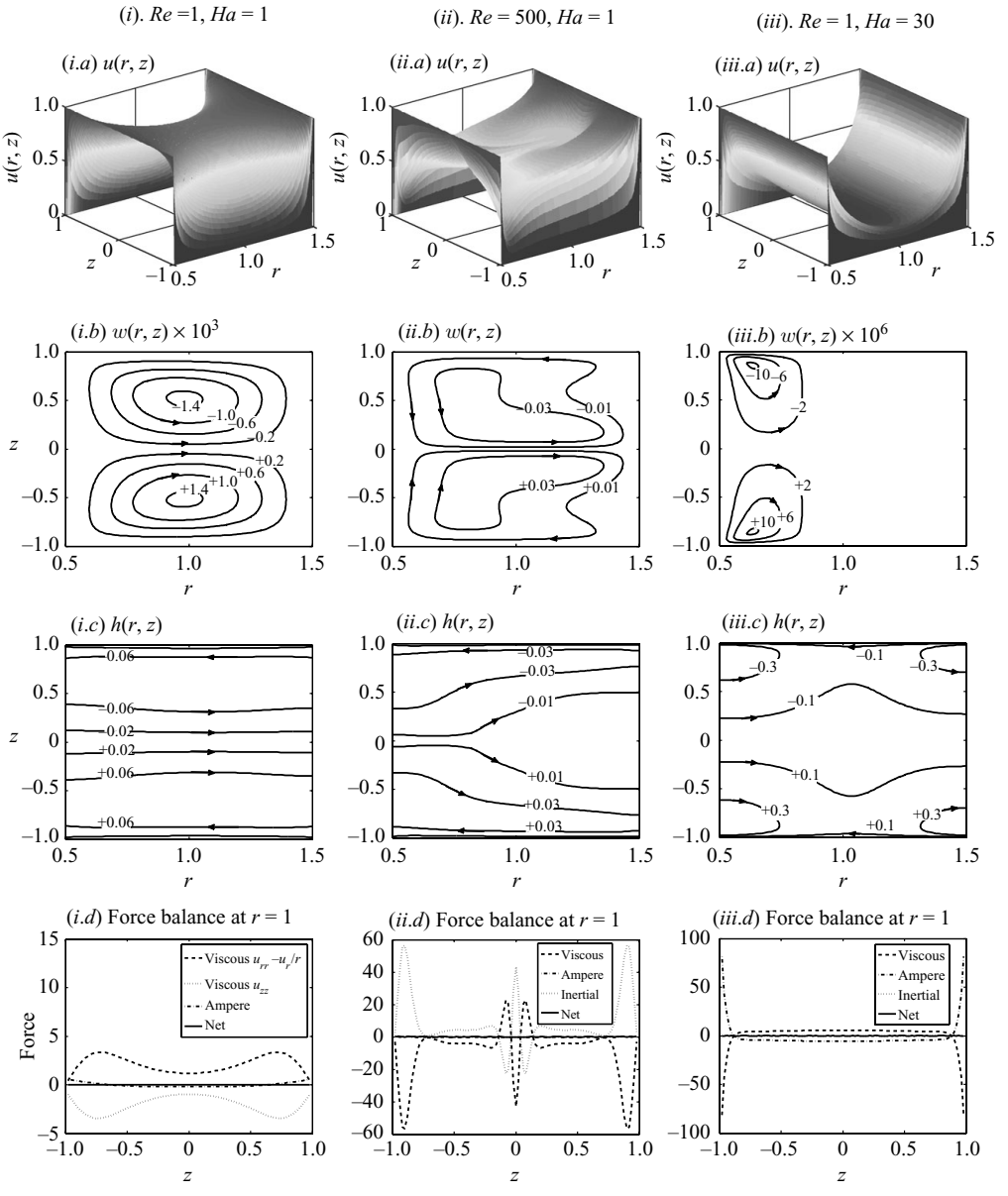

FIGURE 8. Calculated structure of TCF in (*i*) viscous ($Re = 1$, $Ha = 1$), (*ii*) inertial ($Re = 500$, $Ha = 1$) and (*iii*) magnetized ($Re = 1$, $Ha = 30$) regimes. (*a*) Normalized angular momentum $u(r, z)$; (*b*) poloidal circulation lines (contours of $w(r, z)$); (*c*) electric current lines (contours of $h(r, z)$); (*d*) balance of toroidal forces at $r = 1$. Calculations are performed using the full system (2.6)–(2.8).

Similar to the case of EDF we can represent the normalized angular momentum $u(r, z)$ in the form (4.10). Then we use the method of averaging along the magnetic field lines to find the radial profile $u_0(r)$. This method results in (4.13) which for TCF reads

$$\frac{\partial^2 u_0}{\partial r^2} - \frac{1}{r}\frac{\partial u_0}{\partial r} - Ha\,u_0 = 0. \tag{5.12}$$

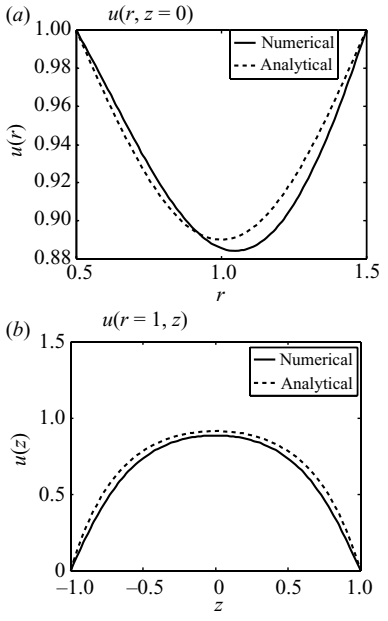

FIGURE 9. Comparison of calculated angular momentum profile $u(r, z)$ (solid lines) with analytical approximation given by (5.7) and (5.8) (dashed lines) in the viscous regime of TCF ($Re = 1$, $Ha = 1$): (a) in the mid-plane of the channel at $z = 0$; (b) at $r = 1$.

The only difference between (5.12) and (4.13) is the absence in (5.12) of the term related to the electrical current drive. As a result, the solution to (5.12) satisfying the boundary conditions (5.1) can be written in a form analogous to (4.14):

$$u_0(r) = \frac{r}{I_1(\sqrt{Ha}(r_2 - r_1))}\left[\frac{u_1}{r_1} I_1(\sqrt{Ha}(r_2 - r)) + \frac{u_2}{r_2} I_1(\sqrt{Ha}(r - r_1))\right]. \tag{5.13}$$

Near the walls at $r = r_{1,2}$ dependence (5.13) becomes

$$u_0(x) \approx u_{1,2} \exp(-\sqrt{Ha}\, x), \tag{5.14}$$

where $x = |r - r_{1,2}|$ is a non-dimensional distance measured from the corresponding wall. Within the side (parallel) layers of thickness $O(Ha^{-1/2})$, the angular momentum drops by factor $e = 2.718$. Thus, if the side layers are much less than the gap between cylinders, i.e. $Ha^{-1/2} \ll r_2 - r_1$, velocity in the bulk of the fluid is practically zero. This result follows from the presence of the steady end caps and Ferraro's iso-rotation law (Ferraro 1937): the angular velocity of a highly conducting fluid tends to be constant along a magnetic field line to minimize the induction effect. In order to use the magnetized regime of TCF in the MRI experiment one has to ensure that the gap between cylinders is less than the side layers, i.e.

$$R_2 - R_1 \lesssim \frac{H}{\sqrt{Ha}}. \tag{5.15}$$

Only if (5.15) is satisfied, the angular velocity of the fluid can be well approximated by (in dimensional units)

$$\Omega(R) = \frac{M_2 - M_1}{R_2^2 - R_1^2} + \left(\frac{M_1 R_2^2 - M_2 R_1^2}{R_2^2 - R_1^2}\right)\frac{1}{R^2}, \tag{5.16}$$

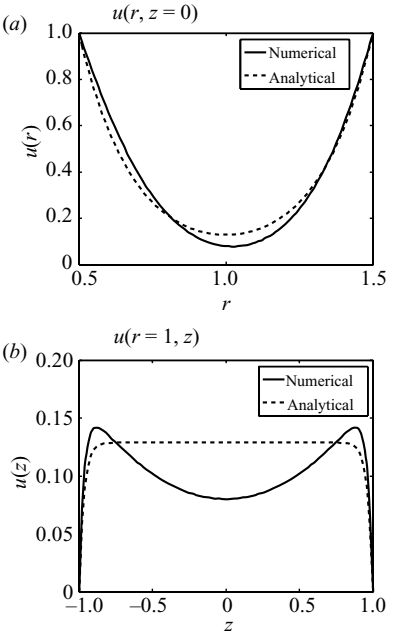

FIGURE 10. Comparison of calculated angular momentum profile $u(r, z)$ (solid lines) with analytical approximation given by (4.10) and (5.13) (dashed lines) in the magnetized regime of TCF ($Re = 1$, $Ha = 30$): (a) in the mid-plane of the channel at $z = 0$; (b) at $r = 1$.

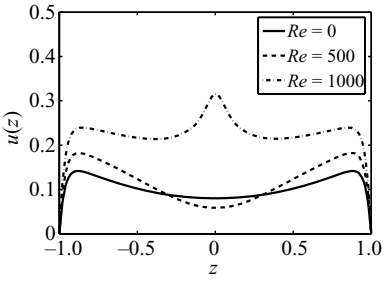

FIGURE 11. Calculated z-profiles of normalized angular momentum $u(r, z)$ at $r = 1$ in TCF for different values of Re at $Ha = 30$.

where $M_1 = \Omega_1 R_1^2$, $M_2 = \Omega_2 R_2^2$ are angular momenta of the inner and outer walls, respectively.

The structure of TCF in the magnetized regime ($Re = 1$, $Ha = 30$) is shown in figure 8(iii.a–d). In this regime the angular momentum profile in the cross-section of the channel (figure 8iii.a) is almost homogeneous in the z-direction and has a parabolic radial dependence as predicted by (5.13). For comparison, the analytical and calculated profiles of u are plotted in figure 10. Figure 8(iii.c) shows the distribution of poloidal electric current in this case.

The dependence of the angular momentum's z-profile on the Reynolds number is shown in figure 11. As one can see, the increase of Reynolds number results in a considerable change of the flow structure. In fact, when $Ha = 30$ and $Re \gtrsim 1000$ the flow turns to inertial regime.

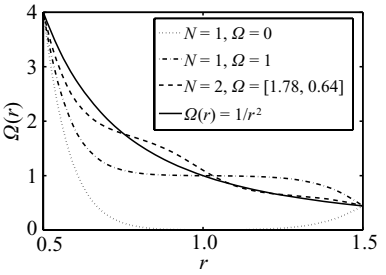

FIGURE 12. Angular velocity profiles at $z=0$ for different number of rotating rings N in the magnetized regime of TCF ($Re=0$, $Ha=100$). Profiles are calculated using system (5.10) and (5.11).

5.6. *Rotating split end caps*

Inequality (5.15) limits the strength of the magnetic field that can be used in the TCF MRI experiment. The highest magnetic field, which does not change rotation profile (5.16) considerably, corresponds to the Hartmann number (see (5.15))

$$Ha \approx \Gamma^2, \tag{5.17}$$

where $\Gamma = H/(R_2 - R_1)$ is the aspect ratio of the channel. The maximum value of the Hartmann number (5.17) can be increased by dividing the end caps into multiple rings that rotate independently. Such idea is realized in the Princeton MRI experiment (Kageyama *et al.* 2004; Ji *et al.* 2004, 2006; Liu 2008*a*,*b*), where two rings are used. Here we consider the effect of these rings on the rotation profile in the magnetized regime of TCF.

First, we study the case of the rigidly rotating end caps (number of rings is $N=1$), assuming that their angular velocity is Ω. Neglecting inertial effects we look for a solution to system (5.10) and (5.11) with $u(r, z)$ satisfying the boundary condition

$$u|_{z=\pm 1} = \Omega r^2.$$

Similar to (4.10) the normalized angular momentum $u(r, z)$ can be approximated as

$$u(r, z) = u_0(r)\frac{\cosh Ha - \cosh(Ha\, z)}{\sinh Ha} + \Omega r^2, \tag{5.18}$$

where

$$u_0(r) = \frac{r}{I_1(\sqrt{Ha}(r_2 - r_1))}\left[\frac{u_1 - \Omega r_1^2}{r_1} I_1(\sqrt{Ha}(r_2 - r)) + \frac{u_2 - \Omega r_2^2}{r_2} I_1(\sqrt{Ha}(r - r_1))\right]. \tag{5.19}$$

Near the walls at $r = r_{1,2}$ angular momentum profile is

$$u(r) \approx (u_{1,2} - \Omega r^2)\exp(-\sqrt{Ha}\,|r - r_{1,2}|) + \Omega r^2. \tag{5.20}$$

Equation (5.20) describes an exponential approach of angular velocity to Ω in the side layers of thickness $O(Ha^{-1/2})$ (see figure 12, case $N=1$). Therefore, we conclude that for Hartmann numbers larger than (5.17), the bulk of the fluid will rotate rigidly with angular velocity Ω. This is not appropriate for MRI experiment.

This result can be generalized to the case with any number of rings N. We note that from the mathematical point of view a circular channel bounded by N pairs of rotating rings (one ring on the top and one on the bottom) is equivalent to the

set of N narrower channels formed by the corresponding pair of rings. The angular momentum profile in each of N channels is approximated by (5.18) and (5.19), with u_1 and u_2 being matching parameters. For the large Hartmann numbers the radial profile of angular velocity has a step-like form (see figure 12, case $N=2$). Profiles closer to (5.16) are obtained if the Hartmann number does not exceed value (for equally spaced N rings)

$$Ha \approx N^2 \Gamma^2, \tag{5.21}$$

which is obviously an improvement compared to (5.17).

Analogous conclusions can be made for other regimes of TCF. The implementation of independently rotating rings at the end caps improves the rotation profile (makes it closer to (5.16)) and broadens the range of Ha and Re appropriate for MRI experiment. Kageyama *et al.* (2004) demonstrated numerically the transition from inertial to viscous regimes of non-magnetized TCF with inclusion of 3, 4 and 5 rings. A similar transition for magnetized TCF with inclusion of two rings was reported by Liu (2008*a*). The simple estimates of the parameters for different TCF regimes and the thickness of the corresponding boundary layers in the case of N rings can be obtained from (5.4) by changing $\Gamma \to N\Gamma$.

6. Conclusions

We have performed the theoretical study of stationary MHD flow structure in an annular channel from the perspective of establishing required parameters for liquid metal MRI experiment. According to obtained results, both electrically driven and Taylor–Couette flows can be used as initial equilibria in MRI experiment. However, different conditions have to be satisfied in both cases to achieve the rotation profiles appropriate for MRI excitation (uniform in axial direction and quasi-Keplerian in radial direction). In the case of TCF, the experimental parameters should satisfy inequality (5.15), while for EDF the opposite condition is necessary (4.16). Besides, the inertial effects have to be reduced in both cases since they influence the rotational profile considerably; this results in condition (4.12). The range of 'good' parameters for MRI experiment is summarized in figure 13.

From figure 13(*a*), one can see that in TCF the 'good' region of parameters is restricted. The limits of this region are determined by the aspect ratio of the channel, $\Gamma = H/(R_2 - R_1)$, and by the number of independently rotating rings in the end caps, N. For the geometry of the Princeton MRI experiment with aspect ratio $\Gamma = 2$ (table 1) and $N=2$, the values of the Hartmann and Reynolds numbers should not exceed $Ha \approx N^2\Gamma^2 \approx 16$ and $Re \approx Ha^2(R_1/H)^2 \approx 16$, respectively. It is well known that MRI in liquid metals does not occur at such small Reynolds numbers (Kageyama *et al.* 2004).

As follows from figure 13(*b*), the 'good' region of EDF is not restricted by the large values of Hartmann number, but it is still limited by the large values of Reynolds number. For the Obninsk MRI experiment (table 1) with $Ha = 100$, the maximum appropriate Reynolds number is $Re \approx 2500$. This is too small for the detection of axisymmetric MRI but can be enough for the observation of non-axisymmetric MRI modes since they have a lower instability threshold (Khalzov *et al.* 2006; Khalzov, Smolyakov & Ilgisonis 2008; Ilgisonis, Khalzov & Smolyakov 2009).

We remark briefly on three issues that might be crucial for the realization of EDF MRI experiment. First, the rotation profile of EDF is predetermined by the drive type: the bulk of the flow corresponds to the so-called Rayleigh line, i.e. the

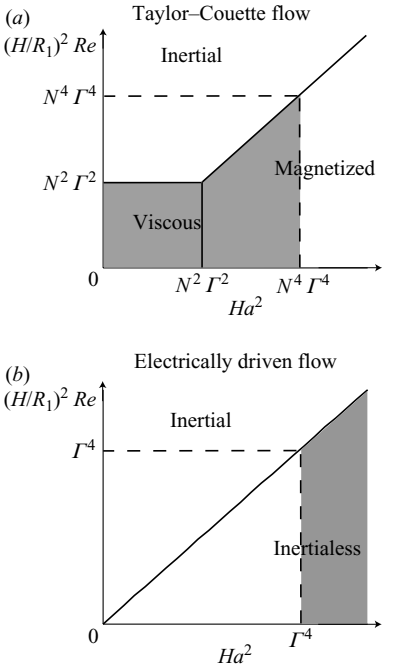

FIGURE 13. Regimes of flows and regions of 'good' parameters in MRI experiments (shaded areas): (*a*) for Taylor–Couette flow; (*b*) for electrically driven flow. $\Gamma = H/(R_2 - R_1)$ is the aspect ratio of the channel and N is the number of rings in the end caps.

flow with constant angular momentum. According to Rüdiger, Schultz & Shalybkov (2003) and Hollerbach & Rüdiger (2005), at this line the MRI threshold is incredibly sensitive to the slightest deviations of the rotation profile, which are certainly present in the experiment due to the boundary layers. However, as discussed by Velikhov *et al.* (2006*a*) such a sensitivity of the Rayleigh line results from minimization of the critical Reynolds number over the magnetic field; so, different points of the threshold curves shown by Rüdiger *et al.* (2003) and Hollerbach & Rüdiger (2005) correspond to different magnitudes of the magnetic field. In the real experiment with the fixed magnetic field such sensitivity of the Rayleigh line does not take place.

The second important issue in EDF is related to the hydrodynamical stability of the parallel boundary layer near the outer wall. The angular momentum profile is radially decreasing in that layer, so that the Rayleigh stability criterion (1.2) is violated and the hydrodynamical instability can develop there. Experimentally, this instability and MRI can be distinguished due to their different spatial localizations: hydrodynamical instability (and resulting turbulence) is localized near the outer wall, while MRI is global and it affects the bulk of the flow. It means that MRI should change the global fluid properties, for example, the effective resistance; the corresponding break of the current-voltage characteristic can be detected experimentally. Obviously, it is not the case for the local hydrodynamical instability. Another way to solve the problem with the side boundary layers is to get rid of them by using the combination of EDF and TCF, which is known as Taylor–Dean flow (Stefani & Gerbeth 2004). An analysis of this flow is beyond the scope of our paper.

The third issue concerns the stability of the Hartmann layers in EDF. The Hartmann boundary layer is known to be subcritically (nonlinearly) unstable (Moresco &

Alboussiére 2003). Transition to turbulence in the Hartmann layer was observed experimentally and confirmed numerically when $150 < Re/Ha < 400$ (Moresco & Alboussiére 2004; Thess *et al.* 2007). In recent experiment with EDF in an annular channel, Moresco & Alboussiére (2004) reported such transition for $Re/Ha = 380$. If EDF is indeed unstable due to the presence of the Hartmann layers, this may bring an additional limitation for the region of "good" parameters of EDF. This is a subject of the further study.

This work is supported in part by the Russian Foundation for Basic Research (project 07-02-00441), the National Science Foundation and the Natural Sciences and Engineering Research Council of Canada.

REFERENCES

Acheson, D. J. & Hide, R. 1973 Hydromagnetics of rotating fluids. *Rep. Prog. Phys.* **36**, 159–221.

Balbus, S. A. 2003 Enhanced angular momentum transport in accretion disks. *Annu. Rev. Astron. Astrophys.* **41**, 555–597.

Balbus, S. A. & Hawley, J. F. 1991 A powerful local shear instability in weakly magnetized disks. I. Linear analysis. *Astrophys. J.* **376**, 214–222.

Balbus, S. A. & Hawley, J. F. 1998 Instability, turbulence, and enhanced transport in accretion disks. *Rev. Mod. Phys.* **70**, 1–53.

Baylis, J. A. & Hunt, J. C. R. 1971 MHD flow in an annular channel: theory and experiment. *J. Fluid Mech.* **48**, 423–428.

Davidson, P. A. & Pothérat, A. 2002 A note on Bödewadt Hartmann layers. *Eur. J. Mech.* B. *Fluids* **21**, 545–559.

Ferraro, V. C. A 1937 The non-uniform rotation of the Sun and its magnetic field. *Mon. Not. R. Astron. Soc.* **97**, 458–472.

Heiser, W. H. & Shercliff, J. A. 1965 A simple demonstration of the Hartmann layer. *J. Fluid Mech.* **22**, 701–707.

Hollerbach, R. & Fournier, A. 2004 End-effects in rapidly rotating cylindrical Taylor–Couette flow. *AIP Conf. Proc.* **733**, 114–121.

Hollerbach, R. & Rüdiger, G. 2005 New type of magnetorotational instability in cylindrical Taylor--Couette flow. *Phys. Rev. Lett.* **95**, 124501.

Ilgisonis, V. I. & Khalzov, I. V. 2007 Magnetorotational instability in a non-uniform magnetic field. *JETP Lett.* **86**, 705–708.

Ilgisonis, V. I., Khalzov, I. V. & Smolyakov, A. I. 2009 Negative energy waves and MHD stability of rotating plasmas. *Nucl. Fusion* **49**, 035008.

Ji, H., Burin, M., Schartman, E. & Goodman, J. 2006 Hydrodynamic turbulence cannot transport angular momentum effectively in astrophysical disks. *Nature* **444**, 343–346.

Ji, H., Goodman, J., Kageyama, A., Burin, M., Schartman, E. & Liu, W. 2004 Magnetorotational instability in a short Couette flow of liquid gallium. *AIP Conf. Proc.* **733**, 21–34.

Kageyama, A., Ji, H., Goodman, J., Chen, F. & Shoshan, E. 2004 Numerical and experimental investigation of circulation in short cylinders. *J. Phys. Soc. Japan* **73**, 2424–2437.

Kaneda, M., Tagawa, T., Noir, J. & Aurnou, J. M. 2005 Variations in driving torque in Couette-Taylor flow subject to a vertical magnetic field. *J. Phys.: Conf. Ser.* **14**, 42–47.

Khalzov, I. V., Ilgisonis, V. I., Smolyakov, A. I. & Velikhov, E. P. 2006 Magnetorotational instability in electrically driven flow of liquid metal: spectral analysis of global modes. *Phys. Fluids* **18**, 124107.

Khalzov, I. V. & Smolyakov, A. I. 2006 On the calculation of steady-state magnetohydrodynamic flows of liquid metals in circular ducts of a rectangular cross-section. *Tech. Phys.* **51**, 26–33.

Khalzov, I. V., Smolyakov, A. I. & Ilgisonis, V. I. 2008 Energy of eigenmodes in magnetohydrodynamic flows of ideal fluids. *Phys. Plasmas* **15**, 054501.

Lakhin, V. P. & Velikhov, E. P. 2007 Instabilities of highly-resistive rotating liquids in helical magnetic fields. *Phys. Lett.* A **369**, 98–106.

Liu, W. 2008*a* Magnetized Ekman layer and Stewartson layer in a magnetized Taylor–Couette flow. *Phys. Rev.* E **77**, 056314.

Liu, W. 2008*b* Numerical study of the magnetorotational instability in Princeton MRI experiment. *Astrophys. J.* **684**, 515–524.

Liu, W., Goodman, J., Herron, I. & Ji, H. 2006 Helical magnetorotational instability in magnetized Taylor–Couette flow. *Phys. Lett.* E **74**, 056302.

Liu, W., Goodman, J. & Ji, H. 2007 Traveling waves in a magnetized Taylor–Couette flow. *Phys. Lett.* E **76**, 016310.

Moresco, P. & Alboussiére, T. 2003 Weakly nonlinear stability of Hartmann boundary layers. *Eur. J. Mech.* B. *Fluids* **22**, 345–353.

Moresco, P. & Alboussiére, T. 2004 Experimental study of the instability of the Hartmann layer. *J. Fluid Mech.* **504**, 167–181.

Müller, U. & Bühler, L. 2001 *Magnetofluiddynamics in Channels and Containers*. Springer.

Noguchi, K. & Pariev, V. 2003 Magnetorotational instability in a Couette flow of plasma. *AIP Conf. Proc.* **692**, 285–292.

Noguchi, K., Pariev, V. I., Colgate, S. A., Beckley, H. F. & Nordhaus, J. 2002 Magnetorotational instability in liquid metal Couette flow. *Astrophys. J.* **575**, 1151–1162.

Pothérat, A., Sommeria, J. & Moreau, R. 2000 An effective two-dimensional model for MHD flows with transverse magnetic field. *J. Fluid Mech.* **424**, 75–100.

Press, W. H., Flannery, B. P., Teukolsky, S. A. & Vettering, W. 1992 *Numerical Recipes in C: The Art of Scientific Computing*, 2nd ed. Cambridge University Press.

Rüdiger, G. & Hollerbach, R. 2007 Comment on 'Helical magnetorotational instability in magnetized Taylor–Couette flow'. *Phys. Lett.* E **76**, 068301.

Rüdiger, G., Schultz, M. & Shalybkov, D. 2003 Linear magnetohydrodynamic Taylor–Couette instability for liquid sodium. *Phys. Rev.* E **67**, 046312.

Silk, J. & Langer, M. 2006 On the first generation of stars. *Mon. Not. R. Astron. Soc.* **371**, 444–450.

Sisan, D. R., Mujica, N., Tillotson, W. A., Huang, Y.-M., Dorland, W., Hassam, A. B., Antonsen, T. M. & Lathrop, D. P. 2004 Experimental observation and characterization of the magnetorotational instability. *Phys. Rev. Lett.* **93**, 114502.

Stefani, F., Gailitis, A. & Gerbeth, G. 2008 Magnetohydrodynamic experiments on cosmic magnetic fields. *Z. Angew. Math. Mech.* **88**, 930–954.

Stefani, F. & Gerbeth, G. 2004 MRI in Taylor–Dean flows. *AIP Conf. Proc.* **733**, 100–113.

Stefani, F., Gundrum, T., Gerbeth, G., Rüdiger, G., Schultz, M., Szklarski, J. & Hollerbach, R. 2006 Experimental evidence for magnetorotational instability in a Taylor–Couette flow under the influence of a helical magnetic field. *Phys. Rev. Lett.* **97**, 184502.

Szklarski, J. 2007 Reduction of boundary effects in the spiral MRI experiment PROMISE. *Astron. Nachr.* **328**, 499–506.

Szklarski, J. & Rüdiger, G. 2007 Ekman–Hartmann layer in a magnetohydrodynamic Taylor–Couette flow. *Phys. Rev.* E **76**, 066308.

Tagawa, T. & Kaneda, M. 2005 Numerical analyses of a Couette–Taylor flow in the presence of a magnetic field. *J. Phys.: Conf. Ser.* **14**, 48–54.

Thess, A., Krasnov, D., Boeck, T., Zienicke, E., Zikanov, O., Moresco, P. & Alboussiére, T. 2007 Transition to turbulence in the Hartmann boundary layer. *GAMM-Mitt.* **30**, 125–132.

Velikhov, E. P. 1959 Stability of an ideally conducting liquid flowing between cylinders rotating in a magnetic field. *Sov. Phys. JETP* **36**, 995–998.

Velikhov, E. P., Ivanov, A. A., Lakhin, V. P. & Serebrennikov, K. S. 2006*a* Magneto-rotational instability in differentially rotating liquid metals. *Phys. Lett.* A **356**, 357–365.

Velikhov, E. P., Ivanov, A. A., Zakharov, S. V., Zakharov, V. S., Livadny, A. O. & Serebrennikov, K. S. 2006*b* Equilibrium of current driven rotating liquid metal. *Phys. Lett.* A **358**, 216–221.

Wendl, M. C. 1999 General solution for the Couette flow profile. *Phys. Rev.* E **60**, 6192–6194.

Youd, A. J. & Barenghi, C. F. 2006 Hydromagnetic Taylor–Couette flow at very small aspect ratio. *J. Fluid Mech.* **550**, 27–42.